

Article

Automating Component-Level Stress Measurements for Inverter Reliability Estimation

Jack Flicker ^{1,*}, Jay Johnson ¹, Peter Hacke ² and Ramanathan Thiagarajan ²

¹ Sandia National Laboratories, Albuquerque, NM 87123, USA; jjohns2@sandia.gov

² National Renewable Energy Laboratory, Lakewood, CO 80401, USA; peter.hacke@nrel.gov (P.H.); ramanathan.thiagarajan@nrel.gov (R.T.)

* Correspondence: jdflick@sandia.gov

Abstract: In the near future, grid operators are expected to regularly use advanced distributed energy resource (DER) functions, defined in IEEE 1547-2018, to perform a range of grid-support operations. Many of these functions adjust the active and reactive power of the device through commanded or autonomous operating modes which induce new stresses on the power electronics components. In this work, an experimental and theoretical framework is introduced which couples laboratory-measured component stress with advanced inverter functionality and derives a reduction in useful lifetime based on an applicable reliability model. Multiple DER devices were instrumented to calculate the additional component stress under multiple reactive power setpoints to estimate associated DER lifetime reductions. A clear increase in switch loss was demonstrated as a function of irradiance level and power factor. This is replicated in the system-level efficiency measurements, although magnitudes were different—suggesting other loss mechanisms exist. Using an approximate Arrhenius thermal model for the switches, the experimental data indicate a lifetime reduction of 1.5% when operating the inverter at 0.85 PF—compared to unity PF—assuming the DER failure mechanism thermally driven within the H-bridge. If other failure mechanisms are discovered for a set of power electronics devices, this testing and calculation framework can easily be tailored to those failure mechanisms.

Keywords: inverter reliability; grid-support functions; stress; lifetime; component degradation



Citation: Flicker, J.; Johnson, J.;

Hacke, P.; Thiagarajan, R.

Automating Component-Level Stress Measurements for Inverter Reliability Estimation. *Energies* **2022**, *15*, 4828. <https://doi.org/10.3390/en15134828>

Academic Editor: Enrique Romero-Cadaval

Received: 31 March 2022

Accepted: 28 June 2022

Published: 1 July 2022

Publisher's Note: MDPI stays neutral with regard to jurisdictional claims in published maps and institutional affiliations.



Copyright: © 2022 by the authors. Licensee MDPI, Basel, Switzerland. This article is an open access article distributed under the terms and conditions of the Creative Commons Attribution (CC BY) license (<https://creativecommons.org/licenses/by/4.0/>).

1. Introduction

In response to increasing photovoltaic (PV) penetration levels on the grid, distributed energy resource (DER) devices—e.g., photovoltaic inverters and energy storage systems (ESS)—are now required to include control modes to improve power quality, in accordance with the U.S. interconnection standard, IEEE 1547-2018 [1]. The set of control modes stipulated in IEEE 1547 includes fixed power factor, voltage-reactive power mode, and an active power limit, providing grid operators with new ways to support distribution voltages [2], participate in load-generation balancing [3], and stabilize the system during power system faults [4].

While the impact of advanced inverter functionality on grid stability and power quality has been well studied [5], the impact of this behavior on inverter lifetime and reliability has not. Operating at off-nominal operating conditions (e.g., non-unity power factor) has been shown to increase switch loss and thermal loss, accelerate device degradation, and reduce overall system lifetime [6–9]. There is a clear tradeoff between PV inverter reliability and grid-level advantages in reliability and power quality for advanced inverter operation.

This also raises major financial and equity questions when grid operators, aggregators, and other third parties operate DER equipment in grid-support modes. Currently, customers are not compensated for reactive power, but reactive power operating modes are potentially reducing the lifetime of their equipment. Additionally, when using voltage-reactive power modes, depending on the customer's geographic location on a distribution

feeder, their DER equipment is likely to operate further from unity power factor (and more often) compared with a customer located closer to the feeder substation. As a result, certain customers are sacrificing more DER lifetime than others to help grid operators perform voltage regulation operations. These issues cannot be resolved through regulations, utility incentives, or compensation without fully understanding the impacts on the DER equipment. This work is a first step in addressing these challenges by quantifying the disparity between DER lifetimes when operating under different reactive power modes.

However, significant barriers exist in quantifying this reduction in unit lifetime using component-level stresses. The first difficulty is instrumenting and monitoring switch stress across the inverter's entire active and reactive power operating envelope. The other is determining the appropriate failure model and lifetime profiles to estimate lifetime reductions.

In this work, we address the first of those challenges and describe a framework for instrumenting and autonomously measuring inverter component stress for a variety of different advanced inverter operating conditions (Figure 1). We demonstrate how those measurements (Step 1) can then be coupled with appropriate advanced inverter operating conditions (either real or expected, Step 2) to create a stress collective (Step 3) [10]. This stress collective can then be combined with an appropriate component lifetime model (Step 4) to determine an effective reduction in useful life of the inverter, due to advanced inverter functionality (Step 5). The primary contributions of this work include (a) creating and demonstrating a flexible framework to model lifetime reductions of DER equipment under different grid-support operating scenarios according to measured component-level stresses, and (b) evaluations of switch and capacitor stress under reactive power modes.

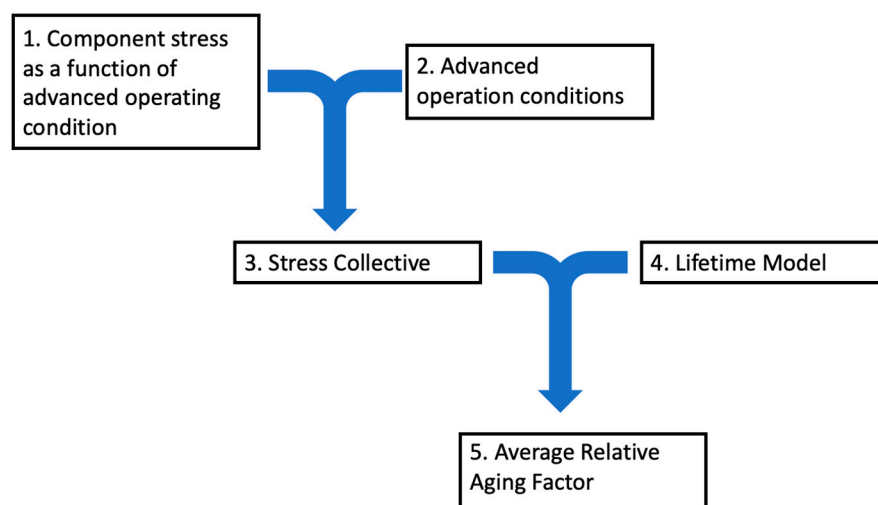


Figure 1. Framework for evaluating PV inverter reduction in useful life based on advanced inverter operation.

The remainder of the paper is structured as follows. Section 2 discusses the laboratory setup for extracting component loss maps as a function of advanced inverter operation; Section 3 presents the loss mapping of three inverters and discusses the meaning of the results; and Section 4 couples the experimental data with component lifetime models to calculate an example reduction in inverter lifetime due to advanced inverter functionality; Section 5 concludes the paper with the importance of the findings and suggested future work.

2. Component Stress Measurements

The first step of the framework shown in Figure 1 is the measurement of component stresses as a function of advanced operating condition. To ensure an accurate parameterization, component stress must be measured under a wide range of advanced operating conditions. This process can be very long and tedious if performed manually. To automate

this process, we altered the System Validation Platform (SVP) [11], which was originally developed as a flexible framework to measure autonomously system-level inverter operations for certification processes. The SVP framework was altered to measure, process, and store component-level loss maps, which can be used as the basis to calculate inverter lifetime reductions as a function of advanced inverter operating condition. Similar in situ approaches could be employed by inverter manufacturers as prognostics tools to calculate component damage, model lifetime, and dynamically calculate time-of-use prices for grid-support functions based on inverter lifetime costs.

2.1. Data Collection

The open-source System Validation Platform (SVP) was initially developed under a Cooperative Research and Development Agreement (CRADA) between Sandia National Laboratories and SunSpec Alliance [11]. This platform has since been expanded by the Smart Grid International Research Facility Network (SIRFN) to include a range of equipment drivers and test scripts for conducting DER interoperability and electrical characterization experiments. The SVP has been used to evaluate test procedures defined in IEEE 1547.1 [12], Underwriters Laboratories 1741 Supplement A [13], a test protocol for IEC TR 61850-90-7 [14], as well as to collect extensive grid-support function operational data to model DER operations [15]. The software platform was written in Python and includes the ability to script actions for multiple hardware devices using a library of device drivers and abstraction layers. Abstraction layers and drivers have been created for PV simulators, grid simulators, DER, data acquisition systems, load banks, and switches [16]. This architecture allows the same test logic (SVP scripts) to be run at multiple laboratories with different equipment.

The SVP allowed flexible measurement of any accessible component inside the inverter, including switches, capacitors, inductors, etc. Using this open architecture as a starting place, a new Tektronix oscilloscope driver and reliability script were created to measure component losses (Figure 2). An SVP script automated the loss calculations for a range of PV irradiance values and power factors, to produce inverter component loss maps under different operating conditions. The SVP was run on a Windows 10 computer networked to the inverters, PV simulator, and Tektronix data acquisition system (DAS). Maps were created for two single-phase inverters and one three-phase.

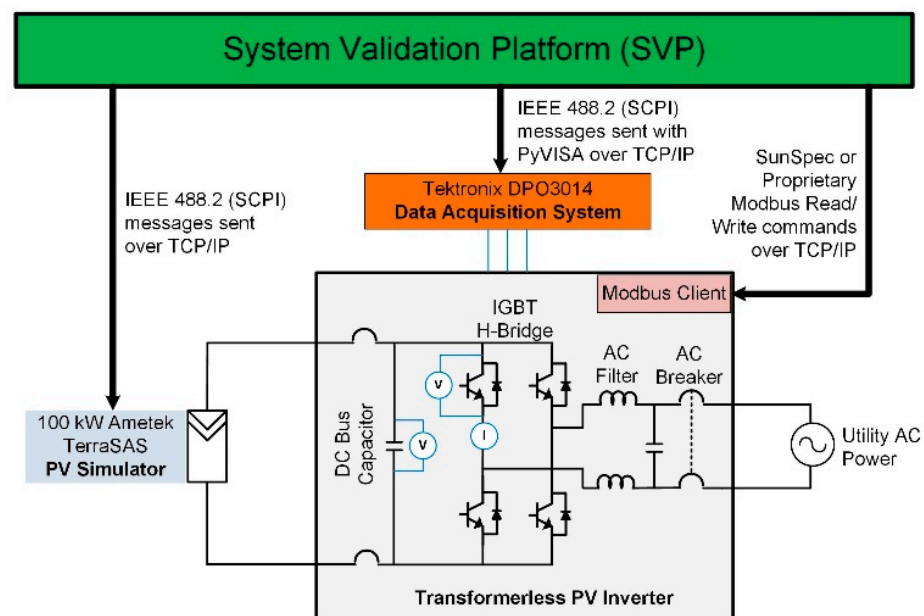


Figure 2. Schematic of the SVP system and component-level reliability measurement of an inverter using an oscilloscope.

2.2. Switch Loss Measurements

In the first experiment, an SVP script measured the switching losses of an inverter by recording switch voltage and current during system operation, as depicted in Figure 2. The inverter tested had a 4-switch H-bridge configuration operating with a variable duty cycle PWM with a frequency ~ 70 kHz. One of the constituent MOSFETs was monitored using a PEM Ltd. CWT micro-Rogowski coil (Long Eaton, Nottingham, UK) and a Tektronix 5210A (Beaverton, OR, USA) isolated voltage probe (Figure 3). These signals were captured by regularly querying the Tektronix DPO3014 oscilloscope through an IEEE 488.2 Standard Commands for Programmable Instruments (SCPI) interface. The SVP driver triggered the oscilloscope according to the user-defined parameters, captured 500 kHz data for each of the channels, and then processed the recorded waveforms in near real-time to calculate switching loss. These results were then saved in the SVP results manifest. A basic flow diagram of the script is shown in Figure 4. The SVP was run on a Windows 10 computer networked to the inverters, PV simulator, and Tektronix Data Acquisition System (DAS).

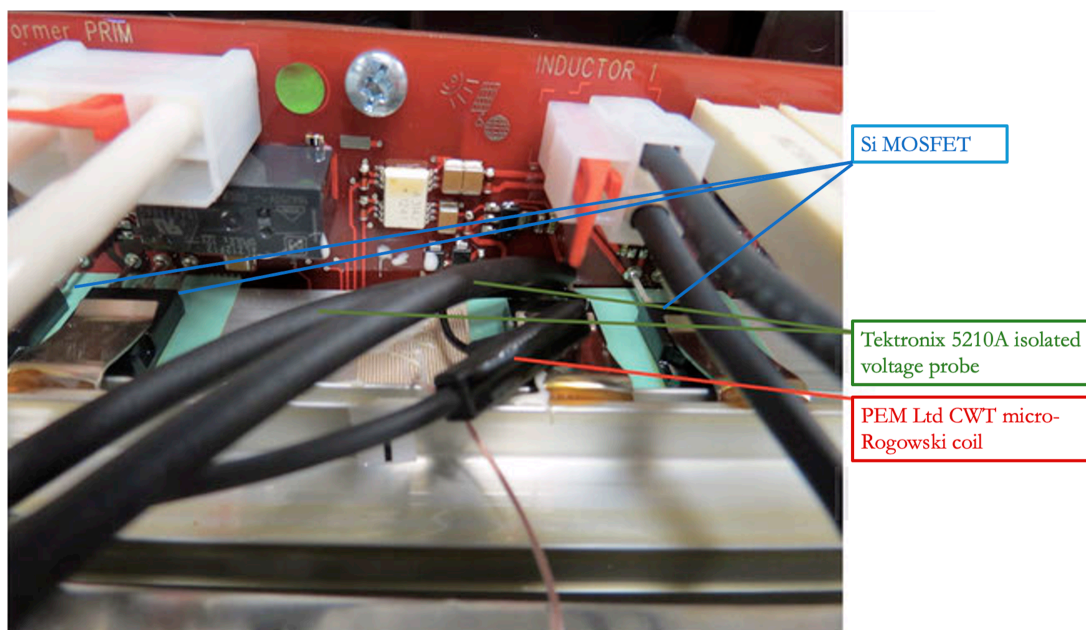


Figure 3. Measurement setup for switch measurements. A single MOSFET in the inverter H-bridge is monitored via isolated voltage probes and a micro-Rogowski current monitor.

Reliability measurement inside SVP data acquisition routine

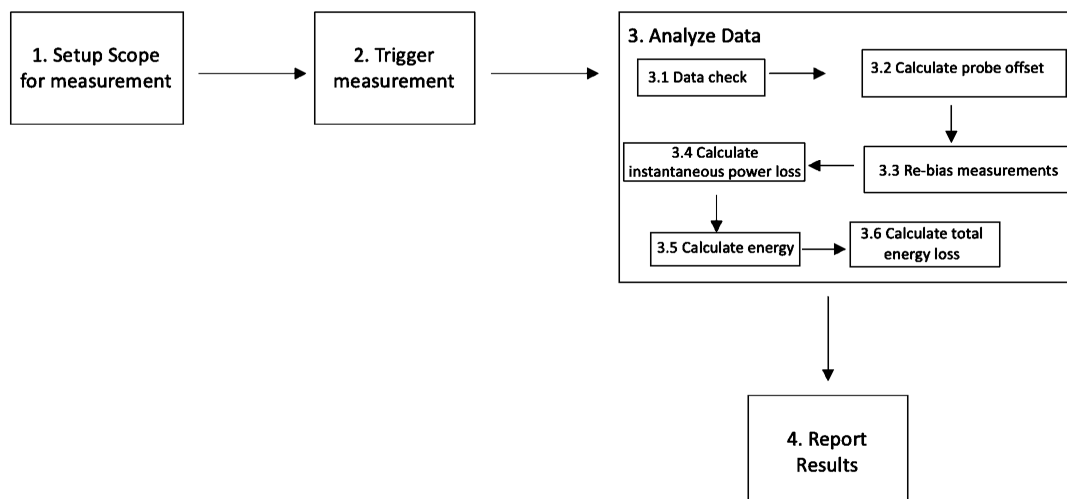


Figure 4. Script to calculate switching loss within SVP.

To calculate switch loss from the oscilloscope measurements (step 3 in Figure 4), the data was first checked to ensure completeness (3.1). This included checking for consistent time steps, NaN values, and signal clipping at either the positive or negative limit of the oscilloscope. If the data was found to be incomplete, information was relayed to the SVP to alter scope setup for an additional measurement at the current system condition. If the data was found to be complete, current probe offset was then calculated (3.2).

Probe offset was calculated by taking the histogram of the absolute value of the current and voltage measurements (Figure 5). It is assumed that the measurement will be approximately bimodal (it can also be multi-modal for more complex inverter topologies). The offset is determined by the mode closest to zero (which is the maximum measurement, typically). Since leakage current is typically negligible in MOSFETs, this mode was assumed to be the probe offset and the measured dataset was shifted by this offset.

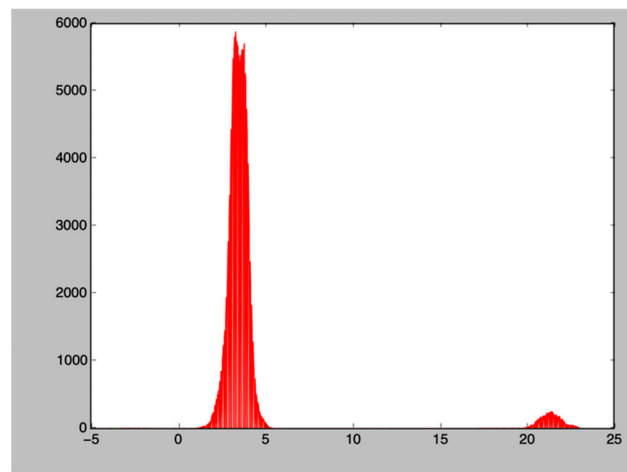


Figure 5. Histogram measurement of current data to determine current offset.

This method of measuring the offset corrects for the offset of the measurement probes but forces the leakage current measurement of the switch to zero, which is undesirable as there may be a (very) small power loss due to leakage loss as a function of inverter state (for example, as bus voltage changes at different power factors). In future versions of the SVP, probe offset will be calculated by taking a measurement with no power flow in the inverter. With no voltage or current applied to the switch, a true probe offset can be calculated. This enables a more complete measurement, at the expense of increasing test time.

Once the offset is removed from the voltage and current waveforms, the instantaneous power at each time point is calculated (3.4) as well as the dissipated energy ($E = P/\Delta t$). A cumulative energy dissipation is then calculated and normalized to 1s (3.6) for equitable comparison between different runs and different devices. Examples of results of each step for a typical dataset is shown in Figure 6. Oscilloscope traces of voltage across the switch and current through the switch were collected ((a) shows an oscilloscope trace for voltage and current for a 60 Hz waveform cycle; (b) shows a switch transition from off to on and on to off). At each measurement point, an instantaneous power dissipation was calculated ((c) shows the instantaneous power dissipation for a single switch cycle for two different power factors). Approximate energy dissipation at each time point was calculated. Cumulative energy dissipation over a 60 Hz cycle was then calculated for the 60 Hz cycle ((d) shows the cumulative energy dissipation for a single switch cycle for two different power factors) and the final dissipated energy over the cycle time was saved to the SVP database.

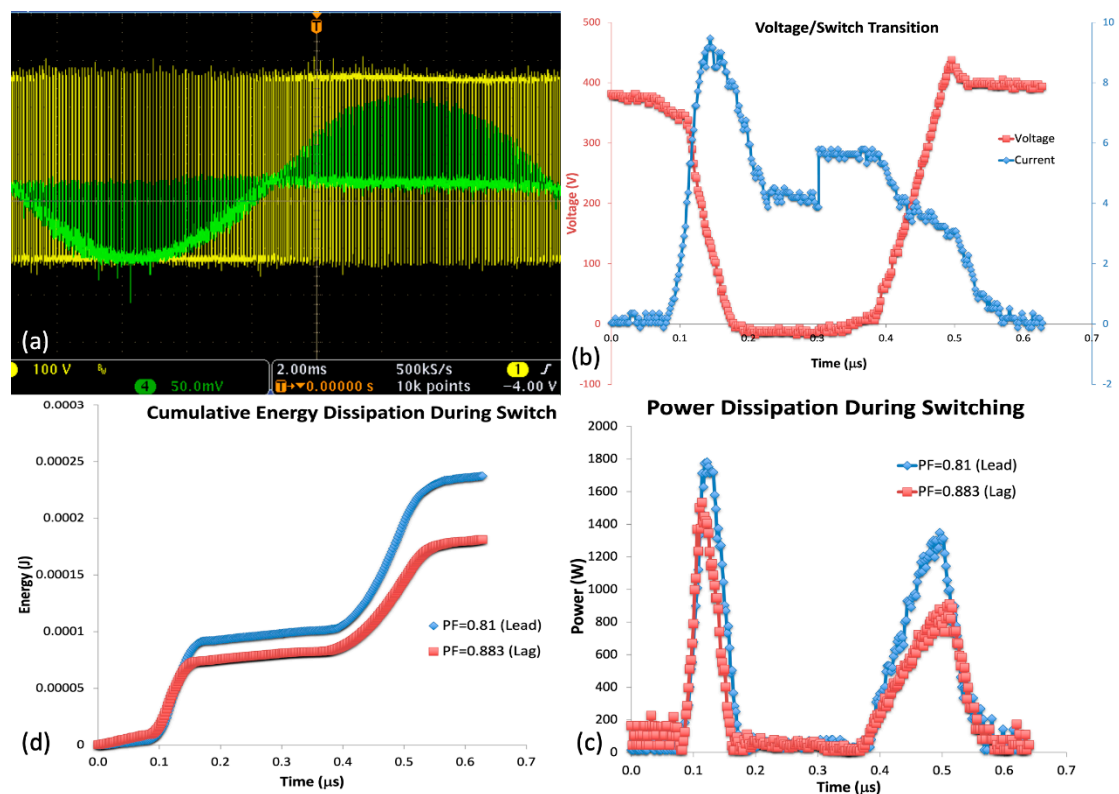


Figure 6. (a) Voltage (yellow) and current (green) waveforms of a MOSFET operating in an inverter. (b) Close-up of a single switch transition of the MOSFET. (c) Power profile of two different PF levels over the switch transitions showing increased power dissipation at crossover. (d) Energy losses can be calculated to be different according to PF.

This autonomous data acquisition routine for the SVP was tested through the instrumentation of a 3-kW single-phase inverter. The switch loss was calculated for inverter operations from -0.85 to $+0.85$ power factor (PF) (corresponding to the maximum and minimum values of the inverter), in 0.01 increments at irradiance levels of 200, 400, 600, 800, and 1000 W/m^2 , using an Ametek TerraSAS PV simulator configured with an EN50530-defined curve with $P_{\text{mp}} = 3200 \text{ W}$ and $V_{\text{mp}} = 460 \text{ V}$. At 1000 W/m^2 , the inverter operated off the maximum power point (MPP) in curtailment mode because the array P_{mp} was 6.67% greater than the nameplate capacity of the DER.

On the AC side, the inverter was connected to the electrical grid. At each operational state, 20 switch measurements were captured to calculate the average and standard deviation for each operational point. Over the five irradiance values, 31 PF setpoints, and 20 measurements per test condition, the experiments took approximately 12 h to run. Using the SVP, the experiments were fully automated, and, after each run, all the data was saved locally on the Windows computer for additional analysis.

2.3. Capacitor Voltage Measurements

Bus capacitors are an at-risk component in inverters because they are subject to stress from internal temperature affects due to ambient operating temperature, as well as self-heating due to voltage ripples on the DC bus. While ambient operational temperature of inverters has been characterized in other projects, voltage and current ripple as a function of operational model is poorly understood. The SVP was utilized to evaluate changes in voltage ripple due to inverter operating state.

This autonomous data acquisition routine was tested through the instrumentation of three different inverters to compare how different inverter designs generate stresses with advanced inverter functionality. The inverters were instrumented to collect voltage on

the internal DC bus using a Tektronix 5210A isolated voltage probe. These signals were captured by regularly querying the Tektronix DPO3014 oscilloscope through an IEEE 488.2 Standard Commands for Programmable Instruments (SCPI) interface.

The SVP driver triggered the oscilloscope according to the user-defined parameters, captured 500 kHz data for each of the channels for a total time of two seconds, and then processed the recorded waveforms in near real-time. For these tests, the inverters were connected to the electrical grid on the AC side and a Sorenson PV simulator on the DC side.

Figure 7 shows an oscilloscope trace of the bus voltage for the inverter while in operation ($PF = 1$, irradiance = 1000 W/m^2). The bus voltage was not steady state and showed large variations ($\sim 30 \text{ V}$) in voltage with a frequency of around 0.6 Hz due to the MPP tracking algorithm of the inverter. For the purposes of capacitor self-heating, deviations in voltage at these frequencies are functionally steady state. For this reason, most capacitor lifetime models utilize the specific 120 Hz ripple component of the bus to calculate reduction in useful lifetime. To identify the 120 Hz component of the bus ripple, the constituent waveform was decomposed into its component frequencies via fast Fourier transform (FFT). This allows windowing where only the amplitudes of specific frequencies are utilized. To identify the 120 Hz component in the waveform, the FFT algorithm was windowed to only track the amplitude of the ripple for frequencies between 110 and 130 Hz .

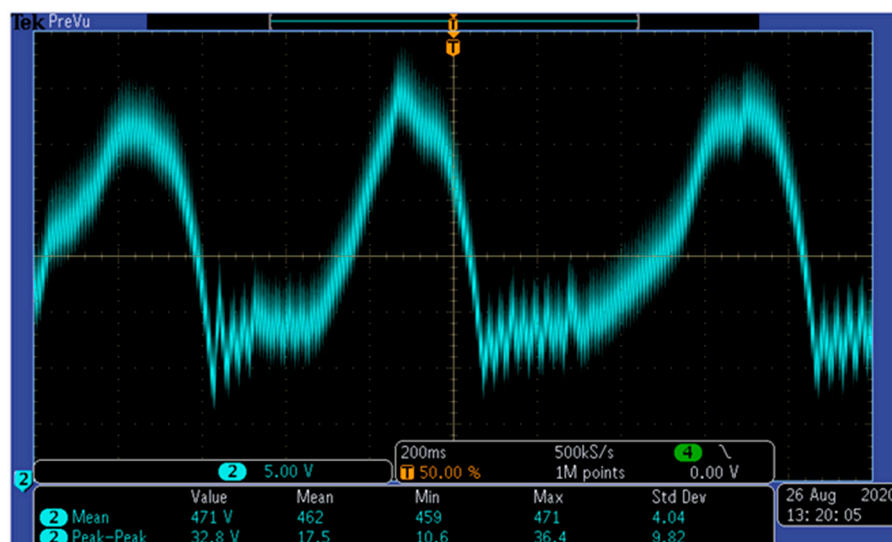


Figure 7. Oscilloscope trace of bus voltage.

3. Results and Discussion

3.1. Switch Loss Measurements

The results for a single-phase inverter are shown in Figure 8. The data points show averaged values for 20 consecutive measurements with error bars denoting the standard deviation in both the x- and y-axes. Error in the measurements is introduced through: (1) time jitter in triggering of the oscilloscope during the AC waveform and (2) differences in actual vs. commanded PF setpoint at the inverter. The left plot shows the system efficiency as measured by the laboratory DAS system. The system level efficiency clearly shows increased loss at increased positive power factor.

Measurements from $400\text{--}1000 \text{ W/m}^2$ had errors in system level efficiency measurements of $<5\%$. The total change in efficiency was $\sim 1\%$, which would produce $\sim 30 \text{ W}$ of loss. The switching-loss measurements (Figure 8, right) had significantly less noise than the system-level measurements and replicated the system-level data. The switching-loss measurements clearly show an increased loss for higher positive power factors for irradiances ranging from 400 to 800 W/m^2 . At low irradiance (200 W/m^2), the inverter has a slightly larger envelope of possible power factor values than the nameplate (± 0.85). This

is most likely due to an issue in the internal inverter control scheme for power factor regulation. At 1000 W/m^2 (turquoise points), the inverter entered a curtailment regime. During curtailment, the inverter demonstrated a relatively constant relationship between power factor and switch loss. This is most likely because, at the apparent power (S) limit of the inverter, an increase in the reactive power of the inverter (Q) necessitates a decrease in real power (P), which tends to keep loss constant. The amount of loss (several J/s) was significantly lower than expected by the system-level measurements and, although it followed the same trend, it cannot fully explain all system level losses. This suggests that other loss mechanisms were present.

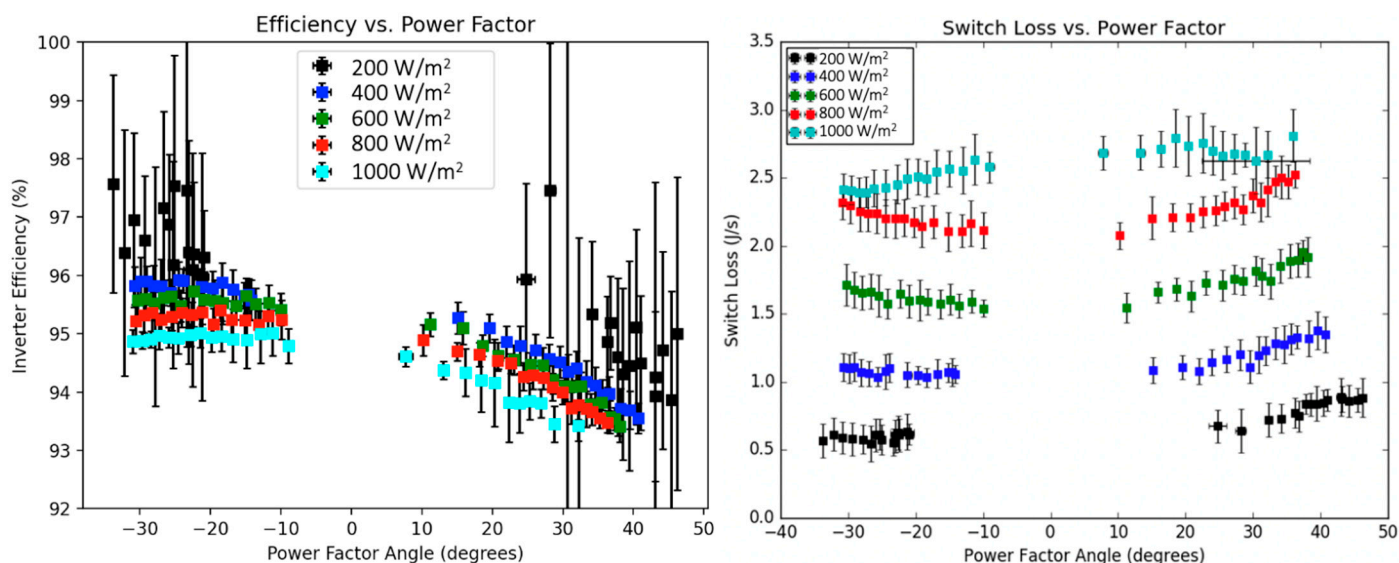


Figure 8. PV inverter losses for a range of PV irradiance levels and power factors. (left) System efficiency vs. power factor angle. (right) switch loss vs. power factor angle.

3.2. Capacitor Voltage Measurements

System-level efficiency data for power factors ranging from -0.85 to 0.85 (the maximum and minimum PF of the inverter) in 0.5 step increments is shown in Figure 9. Each measurement point is the average and standard deviation of five separate measurements. Comparison of the three different devices (Device 1, a single-phase inverter from Manufacturer A; Device 2, a single-phase inverter from Manufacturer B; and Device C, a three-phase inverter from Manufacturer B) showed significant differences in system efficiency when comparing different power factors. Device 3 (right) showed significantly higher efficiency (a $\sim 2\%$ increase) at unity power factor, compared to the single-phase devices. It also had the largest slope with an efficiency ranging from 99.5% (at high negative PF and low irradiance) to a low of 96% (at high positive PF and high irradiance). This behavior was the opposite to Device 2, where the maximum efficiency occurred at high positive PF with high irradiance. Device 1 showed a much smaller dependence on irradiance than Devices 2 and 3. This behavior represents a function of control of the devices as well as differences in topology.

For example, zero voltage switching schemes are optimized for voltage/current crossover at unity power factor. Phase shifting of voltage and current relative to one another (as power factor changes) can result in different losses as a function of power factor. Additionally, LC filtering design choices can result in different loss profiles according to irradiance and power factor. Finally, circuit topology can have an effect. A simple H-bridge inverter would have a different loss profile than a H5 inverter due to the operation of the additional switch [17].

Three devices were tested: a 3-kW single-phase inverter from Manufacturer A (Device 1), a 3-kW single phase inverter from Manufacturer B (Device 2), and a 24-kW three-phase inverter also from Manufacturer B (Device 3). In the case of the 3-kW inverters, one

TerraSAS channel was used (3200 W max), but eight channels were used with the 24-kW three-phase inverter (25.6 kW max).

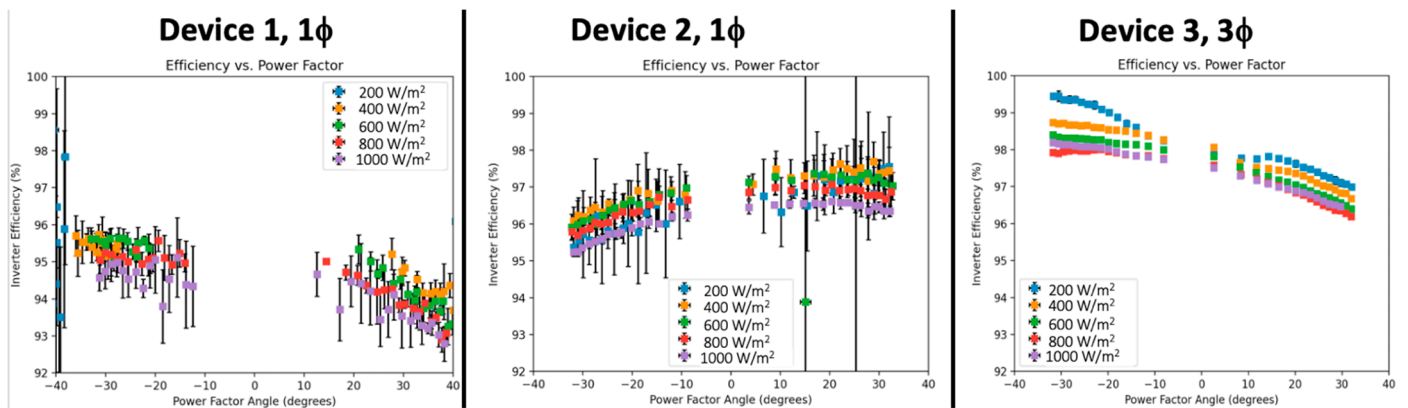


Figure 9. Efficiency measurements for different power factors and irradiance levels for Device 1, a single-phase inverter from manufacturer A (left), Device 2, a single-phase inverter (middle) from Manufacturer B, and Device 3, a three-phase inverter (right) from Manufacturer B.

The results for voltage measurement are shown in Figure 10. The voltage magnitudes (top row) of Devices 1 and 2 show no clear dependence on system irradiance, except for points taken at 1000 W/m² (purple), when the devices entered the curtailment regime. Curtailment by the inverters resulted in a significant increase in bus voltage that was heavily dependent on power factor, with a minimum voltage at near-unity power factors and increased voltage at both positive and negative power factor angles. For Device 1, the bus voltage increased from 465 V to 522 V (12.2%), while Device 2 increased from 465 V to 512 V (10.1%). Unlike the single-phase devices, the three-phase device (Device 3) showed a dependence of bus voltage on irradiance, with increasing irradiance resulting in increasing bus voltage. The three-phase device similarly exhibited a dependence of bus voltage on power factor when curtailing at 1000 W/m². In this case, the bus voltage increased from 493 V to 528 V (7.5%), which was slightly lower than the single-phase devices. In general, none of the devices showed a clear dependence of voltage magnitude on PF, except at full irradiance when the devices entered curtailment mode. In this case, all the inverters showed a large increase in voltage as a function of PF, which may result in increased voltage stress to devices when the inverter is at non-unity PF and in curtailment.

The 120 Hz voltage ripple component of the bus voltage is shown in the bottom row in Figure 10. As expected, Device 3, being a three-phase device, did not show any dependence on PF for voltage ripple, and the magnitude of that ripple was extremely low due to the canceling of ripple on the DC bus. Similarly, Device 2 did not have a dependence of voltage ripple on either irradiance or PF. Device 2 showed increasing voltage ripple with increasing irradiance. There was little relationship between voltage ripple and PF for this device.

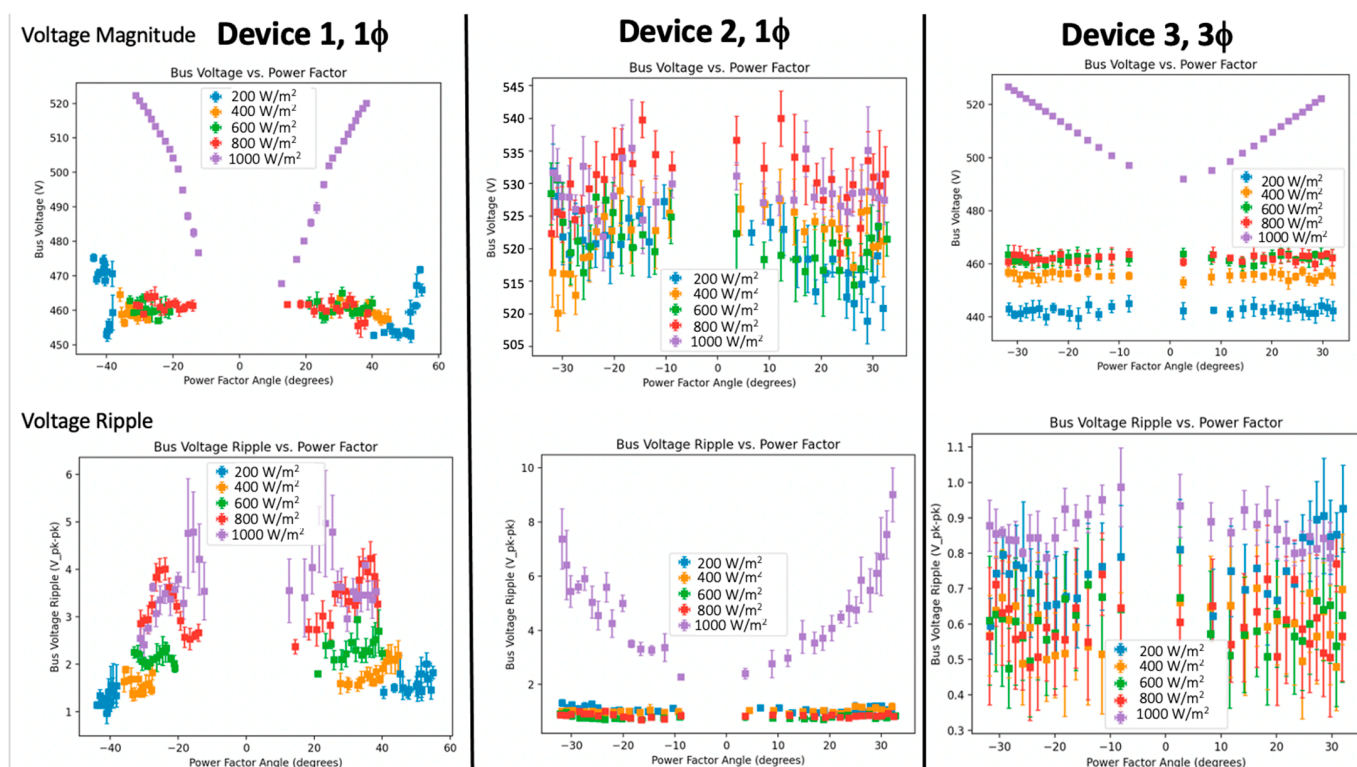


Figure 10. DC Bus voltage magnitude (**top**) and voltage ripple (**bottom**) measurements for different power factors and irradiance levels for Inverter A single-phase inverter (**left**), and Inverter B single-phase inverter (**middle**) and Inverter B three-phase inverter (**right**).

4. Lifetime Estimation

Lifetime modeling of any electronic component is typically a pairwise comparison between states. It can compare two similar devices that are subject to different operational conditions, or carry out a theoretical comparison between the same device subject to different operational conditions. We have developed a framework for evaluating the relative lifetime of two inverters (these can be two distinct inverters or subject to different operational conditions) or nominally the same inverter. This framework, shown in Figure 11, utilizes experimental component level stress, paired with the expected operation of the unit in the field, and an applicable lifetime model, to compare the relative degradation between two different inverters.

We considered two inverters: Inverter A, denoted by a purple star, which operates on one bus in a simulated system (the IEEE 8500-node test feeder [9] is shown as an example but the framework can be applied to any system), as shown in Figure 11, and Inverter B, denoted by a blue star operating at some other location on the system. Due to their different locations in the system, these two inverters have different operating points over a given period. This is because many autonomous grid-support functions, such as volt-var, act on local measurements, such as system voltage, and not globally throughout the system, for example frequency. This operational mission profile can be a time-domain measurement or histogram of operational states (as shown in Figure 11). These operational mission profiles can be paired with the experimental component stress maps described previously, to transform the advanced inverter mission profile into a component stress profile. The component stress can then be paired with an appropriate lifetime model to transform the component stress profile into a collection of acceleration factors. A simple weighted average can then be used to calculate an average acceleration factor comparison between the inverter units.

This process is generic to any failure mechanism that impacts inverter lifetime, although for the failure mechanisms to impact overall system lifetime, the example mecha-

nism must be the relevant limiting failure mechanism for inverter lifetime. We used this framework to derive the expected reduction in inverter useful life via the experimental measurement of switch loss as a function of the power factor, coupled with a thermally driven failure mechanism determined by switch junction temperature.

Although switch failure is a significant failure mechanism in inverters [18] and thermally activated degradation is significant in chip-based (as opposed to package-based) failure mechanisms, especially in emerging technologies such as GaN HEMTs [19,20] and SiC MOS structures [21], there are many other competing failure mechanisms (e.g., capacitor wear-out, contactor failure, die-attach failure). Whether this specific failure mechanism is predominant depends on many factors including actual environmental stress (thermal and electrical), system design, and device usage. However, the framework for evaluation shown in Figure 11 is broadly applicable to different operating modes and failure mechanisms when incorporating the appropriate measurements, fielded operational states, and reliability models.

Capacitors, especially, are a primary cause of failure in inverters [22]. However, we focused on switch loss because the experimental data for switch loss (Figure 8) shows a clear dependence of component stress on power factor. The framework shown in Figure 11 calculates an acceleration factor based on different applications of advanced inverter operation (regardless whether that component stress is a lifetime-limiting stress). If there is no difference in component stress on operation, then the acceleration factor due to advanced inverter operation would always be unity.

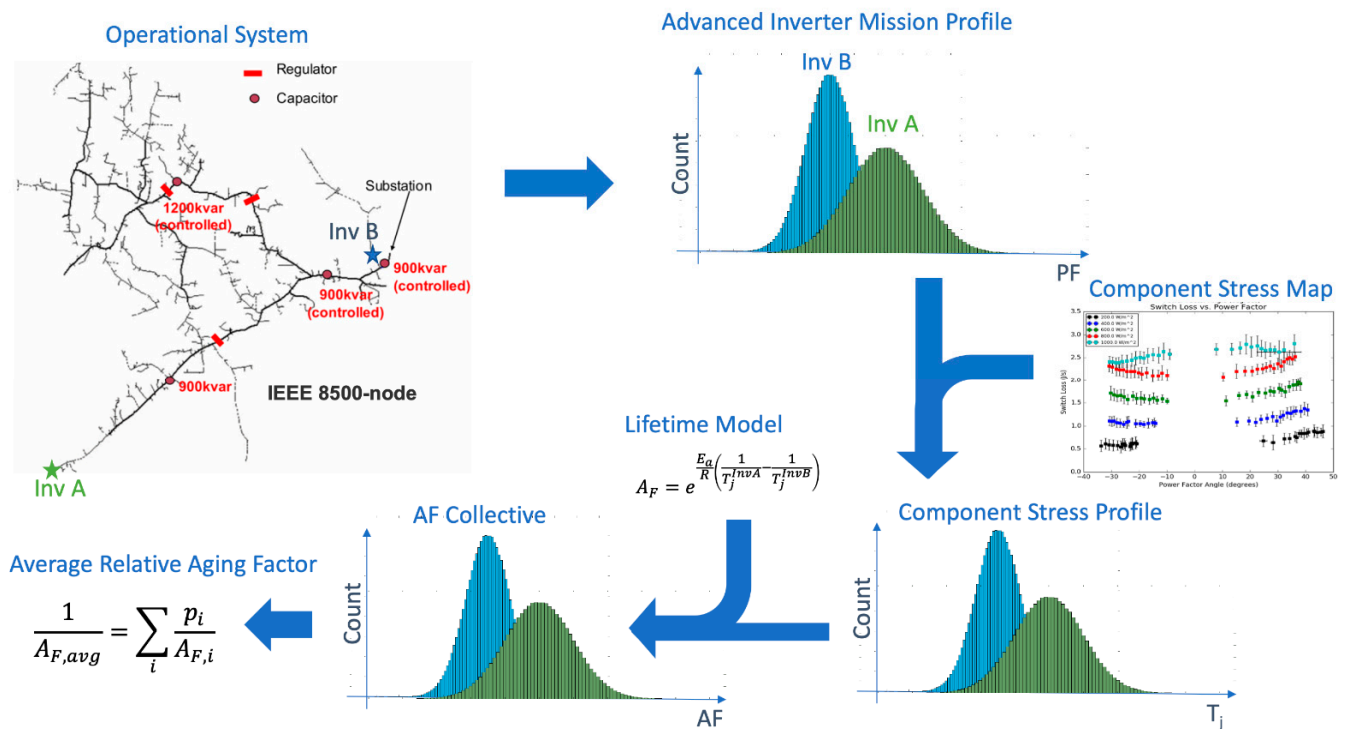


Figure 11. Framework for determination of average inverter acceleration factor. An inverter in a system has a given profile of advanced inverter functionality. This profile can be paired with a component loss map determined experimentally to derive an ensemble of component stress over the profile period. This stress can be translated into a collective of acceleration factors and an average acceleration factor can be derived.

While it is not possible to calculate a realistic reduction in component or inverter lifetime without detailed information on the operational characteristics of the device (e.g., long-term temporal grid-support function parameters, irradiance, and local terminal voltage determined via field measurement or modeling), simplified estimations can be made

using this data along with a few assumptions. For instance, if two example devices are considered that operate throughout their lifetimes at fixed power factor, then it is possible to calculate a relative acceleration factor due to this functionality using ambient temperature and irradiance data, without detailed knowledge of operational system behavior obtained by either historical monitoring of the system or detailed power system simulations.

As an example of this, we utilized the switch loss data collected in Section 3 (Figure 8) to calculate a possible reduction in useful life of two inverters due to thermal stress (driven by increased loss) in a high-side switch in the H-bridge. We considered two inverters, Inverter A, which operates at PF = 1, and Inverter B, which operates at PF = +0.85 (4th quadrant, under-excited).

In this paper, we assume inverter failures are due to switch loss from thermal damage. For a thermally driven process in the switch, the temperature rise in the junction at a steady-state condition due to loss can be calculated by (1) to give a time-based component stress profile.

$$T_j(t) = T_{amb}(t) + P_{loss}(t) \cdot R_{th}, \quad (1)$$

where T_j is the junction temperature in Kelvin, T_{amb} is the ambient temperature in Kelvin, P_{loss} is the switch loss in Watts, and R_{th} is the junction to case thermal resistance in K/W. We consider switching loss as the main component of P_{loss} [23] however, other loss components in the switch (blocking, conduction, etc.) can easily be incorporated using the constituent equations (the dominant loss mode is a function of the switch technology, R_{dson} , and switching frequency).

If T_j is calculated for two systems ($T_j^{Inv A}$ and $T_j^{Inv B}$), then a relative acceleration factor (A_F) for each time step can be found, assuming an Arrhenius model (2).

$$A_F(t) = e^{\frac{-E_a}{k} \left(\frac{1}{T_j^{Inv A}} - \frac{1}{T_j^{Inv B}} \right)}, \quad (2)$$

where k is Boltzmann's constant (8.617×10^{-5} eV/k) and E_a is the activation energy for the failure mechanism (in eV).

For a varying junction temperature due to changes in P_{loss} and T_{amb} , (2) will yield a varying acceleration factor. This distribution of acceleration factors is known as a stress collective [10] and an average acceleration factor can be calculated by a weighted average (3).

$$\frac{1}{A_F^{avg}} = \sum_i \frac{p_i}{A_{F,i}} \quad (3)$$

where p_i is the relative shares (weighting) of a given acceleration factor ($A_{F,i}$).

We considered the acceleration factor between the two inverters (Inverter A at PF = 1, and Inverter B at PF = +0.85), for Albuquerque, NM using 15-min ambient temperature and irradiance data for a typical metrological year (TMY2019) from the National Solar Radiation Database (NSRD) [24].

For each time step in the TMY2019 dataset, NSRD data for ambient temperature (T_{amb}) was used directly in (1). Irradiance values from the NSRD data at each time step were used to extract switch loss (P_{loss}) at a given irradiance through the interpolation of experimental data, shown in Figure 8. Interpolation of experimental data was carried out using MATLAB's griddata function and yielded an approximately linear relationship at a given power factor between P_{loss} and irradiance (bounded by the curtailment of the inverter in high irradiance conditions). A thermal resistance value of 0.5 K/W was assumed (which represents an excellent thermal dissipation). Although activation energy is process specific, an activation energy of 0.8 eV was assumed, which is consistent with failure analysis for semiconductors (e.g., MIL-HDBK-217F [25]).

The calculated values of junction temperature (T_j) at each time step for Inverter A and Inverter B were utilized in (2) to give an acceleration factor between inverters at each time step (AF collective). The AF collective was then used to find an average acceleration factor using (3).

Using these values, an average acceleration factor between the two devices was calculated at 1.0015, indicating a 1.5% faster degradation for Inverter B operating at $PF = +0.85$ compared to Inverter A operating at unity. If the inverter is assumed to have a 20-year lifetime, this would mean that the Inverter B operating at $PF = +0.85$ would fail 3-months earlier on average. As $PF = +0.85$ is the most stressful operational condition, this may represent a worst-case reduction in useful life based on this specific failure mechanism.

5. Conclusions

In this work, we have demonstrated the utility of the SVP framework to evaluate reliability of advanced inverter functions, using automated reliability measurements to parameterize component stress as a function of system operational state. We have described a method of incorporating traditional reliability measurement equipment (e.g., oscilloscope) as a data acquisition unit for the SVP, and utilized this framework to measure inverter switch loss as a function of power factor and irradiance level. We evaluated capacitor stress as a function of irradiance and power factor for three devices, two 3-kW single-phase inverters and a 24-kW three-phase inverter.

The utilization of the SVP as a tool for reliability measurements allows autonomous data collection over many operating conditions. This allows detailed loss maps to be developed. With suitable knowledge of mission profile for advanced inverter functionalities and component lifetime models based on relevant failure mechanisms, this data can be used to calculate reduction in inverter lifetime based on advanced inverter functionality mission profile and a relevant reliability model.

An example of evaluating proposed inverter aging due to operation of advanced inverter functions was utilized using these component-level measurements with appropriate component lifetime models. Considering two equivalent inverters, one operating at unity power factor (considered to be nominal) and one operating at $PF = +0.85$, the relative aging increase was shown to be only 1.5%. This provides a baseline for calculating the possible monetization of advanced inverter functionality as a tool for grid support, since it directly relates a grid support profile to a reduction in useful life of the inverter. In this specific case (switch loss with a thermally driven mechanism comparing a unity power factor inverter to an inverter at maximum power factor), the reduction in useful life was rather minor and the global benefits to the grid certainly outweigh the decrease in reliability (especially as the actual fielded operation of grid support in extent and duration will be less than the simple case examined here). However, this framework of experimental characterization with reliability modeling can be utilized for a wide variety of system operational behaviors, component stressors, and failure mechanisms, and depending on the specific use conditions and failure mechanisms, significantly different aging rates (and thus monetary trade-offs) could result.

Future work is ongoing to use this framework for more realistic advanced inverter operational profiles. This involves pairing grid modelling to extract the inverter operational profile with the experimental reliability characterization described here to extract more realistic data for reduction in useful life. Sensitivity analysis of the assumptions described here (activation energy, thermal resistance, etc.) is also ongoing, to determine the broad picture of inverter reliability due to advanced operating functions.

Author Contributions: Conceptualization, J.F.; Data curation, J.J. and R.T.; Formal analysis, J.J. and P.H.; Funding acquisition, J.F.; Investigation, J.F.; Methodology, J.J., P.H. and R.T.; Project administration, J.F.; Writing—original draft, J.F. All authors have read and agreed to the published version of the manuscript.

Funding: This material is based upon work supported by the U.S. Department of Energy's Office of Energy Efficiency and Renewable Energy (EERE) under the Solar Energy Technologies Office Award Number 34217. Sandia National Laboratories is a multimission laboratory managed and operated by National Technology & Engineering Solutions of Sandia, LLC, a wholly owned subsidiary of Honeywell International Inc., for the U.S. Department of Energy's National Nuclear Security Administration under contract DE-NA0003525.

Institutional Review Board Statement: Not applicable.

Informed Consent Statement: Not applicable.

Conflicts of Interest: The authors declare not conflict of interest.

References

1. IEEE Standard for Interconnection and Interoperability of Distributed Energy Resources with Associated Electric Power Systems Interfaces; IEEE: Piscataway, NJ, USA, 2018.
2. Summers, A.; Johnson, J.; Darbali-Zamora, R.; Hansen, C.; Anandan, J.; Showalter, C. A comparison of DER voltage regulation technologies using real-time simulations. *Energies* **2020**, *13*, 3562. [CrossRef]
3. Kenyon, R.W.; Bossart, M.; Marković, M.; Doubleday, K.; Matsuda-Dunn, R.; Mitova, S.; Julien, S.A.; Hale, E.T.; Hodge, B.-M. Stability and control of power systems with high penetrations of inverter-based resources: An accessible review of current knowledge and open questions. *Sol. Energy* **2020**, *210*, 149–168. [CrossRef]
4. Talha, M.; Raihan, S.; Rahim, N.A. PV inverter with decoupled active and reactive power control to mitigate grid faults. *Renew. Energy* **2020**, *162*, 877–892. [CrossRef]
5. Smith, J.; Sunderman, W.; Dugan, R.; Seal, B. Smart inverter volt/var control functions for high penetration of PV on distribution systems. In Proceedings of the 2011 IEEE/PES Power Systems Conference and Exposition, Phoenix, AZ, USA, 20–23 March 2011; pp. 1–6.
6. Flicker, J.; Gonzalez, S. Performance and reliability of PV inverter component and systems due to advanced inverter functionality. In Proceedings of the 2015 IEEE 42nd Photovoltaic Specialist Conference (PVSC), New Orleans, LA, USA, 14–19 June 2015; pp. 1–5.
7. Anurag, A.; Yang, Y.; Blaabjerg, F. Thermal Performance and Reliability Analysis of Single-Phase PV Inverters with Reactive Power Injection Outside Feed-In Operating Hours. *IEEE J. Emerg. Sel. Top. Power Electron.* **2015**, *3*, 870–880. [CrossRef]
8. Ma, K.; Liserre, M.; Blaabjerg, F. Reactive Power Influence on the Thermal Cycling of Multi-MW Wind Power Inverter. *IEEE Trans. Ind. Appl.* **2013**, *49*, 922–930. [CrossRef]
9. Yang, Y.; Blaabjerg, F.; Wang, H.; Simões, M.G. Power control flexibilities for grid-connected multi-functional photovoltaic inverters. *IET Renew. Power Gener.* **2016**, *10*, 504–513. [CrossRef]
10. Stadler, R.; Maurer, A. Methods for Durability Testing and Lifetime Estimation of Thermal Interface Materials in Batteries. *Batteries* **2019**, *5*, 34. [CrossRef]
11. Johnson, J.; Fox, B. Automating the Sandia advanced interoperability test protocols. In Proceedings of the 40th IEEE PVSC, Denver, CO, USA, 8–13 June 2014; pp. 8–13.
12. Ninad, N.; Apablaza-Arancibia, E.; Bui, M.; Johnson, J.; Gonzalez, S.; Darbali-Zamora, R.; Cho, C.; Son, W.; Hashimoto, J.; Otani, K.; et al. PV Inverter Grid Support Function Assessment using Open-Source IEEE P1547. 1 Test Package. In Proceedings of the 2020 47th IEEE Photovoltaic Specialists Conference (PVSC), Calgary, AB, Canada, 15 June–21 August 2020; pp. 1138–1144.
13. Johnson, J.; Apablaza-Arancibia, E.; Ninad, N.; Turcotte, D.; Prieur, A.; Ablinger, R.; Brindlinger, R.; Moore, T.; Heidari, R.; Hashimoto, J.; et al. International development of a distributed energy resource test platform for electrical and interoperability certification. In Proceedings of the 2018 IEEE 7th World Conference on Photovoltaic Energy Conversion (WCPEC) (A Joint Conference of 45th IEEE PVSC, 28th PVSEC & 34th EU PVSEC), Waikoloa, HI, USA, 10–15 June 2018; pp. 2492–2497.
14. Johnson, J. *Collaborative Development of Automated Advanced Interoperability Certification Test Protocols for PV Smart Grid Integration*; Sandia National Lab. (SNL-NM): Albuquerque, NM, USA, 2014.
15. Hernandez-Alvidrez, J.; Johnson, J. Parametric PV grid-support function characterization for simulation environments. In Proceedings of the 2017 IEEE 44th Photovoltaic Specialist Conference (PVSC), Washington, DC, USA, 25–30 June 2017; pp. 2153–2158.
16. Johnson, J. SVP Energy Lab Testing Script. Available online: https://github.com/jayatsandia/svp_energy_lab/tree/dev3.7 (accessed on 21 January 2021).
17. Albalawi, H.; Zaid, S.A. An H5 Transformerless Inverter for Grid Connected PV Systems with Improved Utilization Factor and a Simple Maximum Power Point Algorithm. *Energies* **2018**, *11*, 2912. [CrossRef]
18. Golnas, A. PV System Reliability: An Operator’s Perspective. Presented at the 38th Photovoltaic Specialists Conference, Austin, TX, USA, 15 August 2012.
19. Zanoni, E.; Meneghini, M.; Meneghesso, G.; Bisi, D.; Rossetto, I.; Stocco, A. Reliability and failure physics of GaN HEMT, MIS-HEMT and p-gate HEMTs for power switching applications: Parasitic effects and degradation due to deep level effects and time-dependent breakdown phenomena. In Proceedings of the 2015 IEEE 3rd Workshop on Wide Bandgap Power Devices and Applications (WiPDA), Blacksburg, VA, USA, 2–4 November 2015; pp. 75–80. [CrossRef]
20. Wu, Y.; Chen, C.-Y.; del Alamo, J.A. Activation energy of drain-current degradation in GaN HEMTs under high-power DC stress. *Microelectron. Reliab.* **2014**, *54*, 2668–2674. [CrossRef]
21. Gurfinkel, M.; Horst, J.C.; Suehle, J.S.; Bernstein, J.B.; Shapira, Y.; Matocha, K.S.; Dunne, G.; Beaupre, R.A. Time-Dependent Dielectric Breakdown of 4H-SiC/SiO₂ MOS Capacitors. *IEEE Trans. Device Mater. Reliab.* **2008**, *8*, 635–641. [CrossRef]
22. Yang, S.; Bryant, A.; Mawby, P.; Xiang, D.; Ran, L.; Tavner, P. An industry-based survey of reliability in power electronic converters. *IEEE Trans. Ind. Appl.* **2011**, *47*, 1441–1451. [CrossRef]

-
23. Xiong, Y.; Sun, S.; Jia, H.; Shea, P.; Shen, Z.J. New Physical Insights on Power MOSFET Switching Losses. *IEEE Trans. Power Electron.* **2009**, *24*, 525–531. [[CrossRef](#)]
 24. Sengupta, M.; Xie, Y.; Lopez, A.; Habte, A.; Maclaurin, G.; Shelby, J. The national solar radiation data base (NSRDB). *Renew. Sustain. Energy Rev.* **2018**, *89*, 51–60. [[CrossRef](#)]
 25. *Military Handbook: Reliability Prediction of Electronic Equipment*; Department of Defense: Washington DC, USA, 1991.